Interfacial water thickness at inorganic nanoconstructs and biomolecules: Size matters

Interfacial water thickness at inorganic nanoconstructs and biomolecules: Size matters

Annalisa Cardellini[a], Matteo Fasano[a], Eliodoro Chiavazzo[a], Pietro Asinari[a,*]

[a]*Dipartimento di Energia, Politecnico di Torino, Corso Duca degli Abruzzi 24, 10129 Torino*

Abstract

Water molecules in the proximity of solid nanostructures influence both the overall properties of liquid and the structure and functionality of solid particles. The study of water dynamics at solid-liquid interfaces has strong implications in energy, environmental and biomedical fields. This article focuses on the hydration layer properties in the proximity of Carbon Nanotubes (CNTs) and biomolecules (proteins, polipeptides and amino acids). Here we show a quantitative relation between the solid surface extension and the characteristic length of water nanolayer (δ), which is confined at solid-liquid interfaces. Specifically, the size dependence is attributed to the limited superposition of nonbonded interactions in case of small molecules. These results may facilitate the design of novel energy or biomedical colloidal nanosuspensions, and a more fundamental understanding of biomolecular processes influenced by nanoscale water dynamics.

Keywords: Water dynamics, Hydration layer, Interfacial phenomena, Molecular dynamics

1. Introduction

Water at solid-liquid nanoscale interfaces shows properties significantly different from those in the bulk region. This altered behavior is manly due to non-

*Corresponding author
Email address: pietro.asinari@polito.it (Pietro Asinari)

bonded interactions with the solid phase, which are able to confine some layers of water molecules and to modify the structural and dynamic characteristics of the solvent at the interface [1]. The solid-liquid interactions at the nanoscale induce water molecules to form a structured solid-like layer (also known as nanolayer or hydration layer/shell [2]) with increased density [3, 4]. Moreover, in such nanoconfined condition the self-diffusivity of water is generally reduced and the viscosity is dramatically increased [5, 6].

Several experimental and modeling techniques have been employed to investigate the peculiar properties of interfacial water. For example, by using nano-ultrasonic technique, Mante and colleagues observed the high mass density and the elastic modulus of water at alumina-water interfaces [7]. The mechanical anomalies of the hydration water layer, including the largely enhanced viscosity and non-squeeze-out fluidity, have been also studied by surface force apparatus [8], scanning force microscopy [9] and atomic force microscopy [10]. Atomistic simulations, e.g. Molecular Dynamics (MD), are also powerful methods for studying the distribution and mobility of nanoconfined water [11, 12]. Recently, MD simulations and theoretical analogies with the properties of supercooled water have unveiled a scaling behavior for the self-diffusion coefficient of water in more than sixty confined configurations [1]. Such scaling behavior has been further validated by recent, independent neutron experiments measuring the mobility of nanoconfined water [13, 14].

A broad variety of energy, environmental and biomedical applications take advantages of the peculiar properties of nanoconfined water [15, 16]. For example, the reduction of water self-diffusion coefficient in the proximity of contrast agents for magnetic resonance imaging leads to significant enhancements in diagnostic performances [17]. Water hydration shell rearrangement has been also identified as a key ingredient for the insertion of anti-cancer drugs into the DNA minor groove [18, 19]. Moreover, the peculiar heat and mass transport properties of nanolayer are responsible for the outstanding thermo-physical properties of nanofluids [20, 21], which are mainly investigated for energy [22] or biomedical [23] applications.

On the other hand, water at solid-liquid interface plays a fundamental role in controlling the activity and functionality of solid nanostructures [24, 25]. In particular, protein folding, molecular recognition, self-assembly and aggregation are strongly influenced by the thickness of water layer confined at the surface [26, 27, 28]. For example, stability and conformation of Amyloid plaques, which are associated with several neurodegenerative diseases such as Alzheimer and Parkinson, are regulated by the quantity of water adsorbed at the surface [29, 30, 31]. The structural changes of dioleoylphosphatidylcholine (DOPC) bilayer are promoted by its progressive hydration [32], and the binding process at protein interfaces is also facilitated by a network between adhesive water molecules at the surface [33]. Moreover, changes in the hydration layer depth around DNA are also observed during the transition from helix to coil configuration [34]. The clustering and aggregation dynamics of suspended nanoparticles (e.g. graphene) are also influenced by the thickness of nanoconfined water [35, 36].

These examples show a crucial role for the water layer at nanoscale interfaces: on one hand, it modifies the overall properties of surrounding liquid; on the other hand, water at nanoscale interfaces strongly influences the dynamics of solid phase itself. Hence, a more quantitative understanding of the extension and properties of the hydration level is fundamental in many emerging nano- and biotechnology applications.

In this article, the characteristic length of water nanolayer (δ) adsorbed at the interface is systematically investigated for Carbon Nanotubes (CNTs) and biomolecules (proteins and amino acids). While the relation between surface chemistry and δ has been clarified in previous studies [1, 15, 37], here the analysis focuses on the link between the size of solid particles and their capability to confine water molecules. MD simulations are first performed to equilibrate the solvated systems; trajectories are then processed and the resulting δ are finally interpreted in the light of the local solid-liquid nonbonded interactions. Results highlight a dependence of the hydration layer thickness on the solid particle size. Specifically, a general law to predict the thickness of hydration layer, and thus the amount of interfacial water, is reported. This approach may help to better

understand both colloidal nanosuspensions properties and biological processes involving nanoconfined water. Moreover, the study of hydration layer around amino acids or small peptides could lead to a more fundamental understanding of aggregation, dynamics and functionality of biomolecules.

2. Methods

2.1. ***Characteristic length of nanolayer***

In bulk conditions, water molecules fluctuate with a kinetic energy proportional to k_BT, where k_B is the Boltzmann constant and T the fluid temperature. Approaching to solid surfaces, instead, the state of agitation of the solvent is restrained by interacting potentials with the atoms of solid phase. Hence, a layer of water molecules characterized by a reduced mobility and a more ordered structure is typically formed at the solid-liquid interface. Such layer is usually called nanolayer or hydration layer [2], whose thickness can be quantified by a characteristic length δ [1], which depends on the confining potential.

In the nanolayer, water dynamics is altered by the solid-liquid effective potential $U_{eff} = U_{vdw} + U_c$, where U_{vdw} and U_c are the van der Waals and Coulomb potentials, respectively. Let us consider the $i-th$ solid atom on the solvent accessible surface and the direction n orthogonal to the solid surface in the proximity of the $i-th$ atom, the solid-liquid effective potential along n can be then computed as:

$$U_{eff}(n) = U_{vdw}(n) + \langle U_c \rangle (n). \tag{1}$$

Here, van der Waals interactions are modeled with a 12-6 Lennard-Jones (LJ) model:

$$U_{vdw}(n) = \sum_{k=1}^{N_n} 4\varepsilon_k \left[\left(\frac{\sigma_k}{r_k} \right)^{12} - \left(\frac{\sigma_k}{r_k} \right)^{6} \right], \tag{2}$$

where ε_k and σ_k are the LJ parameters obtained through the Lorentz-Berthelot combination rules between the generic water oxygen with coordinate n and the center of the $k-th$ nearest neighbor. r_k is the Euclidean distance between water

oxygen along n direction and the $k-th$ atom. Note that N_n is the amount of nearest neighbors of the $i-th$ atom within the selected computational cut-off radius r_c, which is chosen such that $U_{eff}(r_c) \approx 0$ and vanishing derivative.

Coulomb potential, instead, takes into account the fluctuations of water dipoles due to thermal agitation. Assuming a Maxwell-Boltzmann distribution of the dipoles orientation, the mean Coulomb potential along n is:

$$\langle U_c \rangle (n) = -E\mu_w \Gamma \left(\frac{E\mu_w}{k_B T} \right), \tag{3}$$

where E, μ_w and Γ are the electric strength, the water dipole momentum (7.50×10^{-32} Cm for SPC/E model [1]) and Langevin function, respectively. It is worth to notice that the adopted SPC/E model represents water as a triatomic molecule, which has a single Lennard-Jones site (oxygen atom) and three point charges (both hydrogen and oxygen atoms). Therefore, the thermal fluctuations of the oxygen atom position are neglected for the calculation of U_{eff}; whereas the thermal fluctuations of water dipole around the equilibrium position are taken into account. For this reason, the ensemble average due to the thermal agitation of water molecules has been adopted only for the electrostatic component.

Once U_{eff} is computed along the n direction in the proximity of the $i-th$ atom, a local characteristic length of water nanolayer δ_i can be evaluated. Following the approach in Reference [1], $\delta_i = n_{i,2} - n_{i,1}$, where $n_{i,1}$ and $n_{i,2}$ are the zeros of equation:

$$U_{eff}(n) + \alpha k_B T = 0, \tag{4}$$

being α related to the degree of freedoms of the water molecules motion. Equation 4 describes a balance between the solid-liquid effective potential (U_{eff}), which causes a reduction of water mobility at the solid-liquid interface, and the kinetic energy of the solvent ($\alpha k_B T$), which weakens the adsorption of water to the solid surface. In particular, $\alpha k_B T$ is constant along n and it may intersect U_{eff} in two points: $n_{i,1}$ and $n_{i,2}$. The zeros of Equation 4 define the distance δ_i, below which the effective potential is stronger than the thermal energy of

water molecules, namely solid-liquid interactions significantly alter water dynamics. In other words, δ_i measures the depth of water layer absorbed to the solid surface.

Once the local characteristic lengths δ_i are evaluated, a weighted mean δ can be computed on the Solvent Accessible Surface (SAS [38]) as:

$$\delta = \frac{\sum_{i=1}^{N} \delta_i S_{loc,i}}{S_{tot}}, \tag{5}$$

where N is the total number of atoms forming the solid geometries, $S_{loc,i}$ the specific SAS of the $i-th$ atom and $S_{tot} = \sum_{i=1}^{N} S_{loc,i}$ the overall SAS. Once the equilibrium configuration of the nanoconfined setup is known, both S_{tot} and $S_{loc,i}$ can be computed from short MD simulations; whereas δ is a characteristic quantity of the geometry (i.e. MD geometry) and nonbonded interactions (i.e. MD force field) of the solid-liquid interface. Since the solvent accessible surfaces obtained from MD trajectories show oscillations in time because of thermal fluctuations, standard deviations of δ can be also estimated for each considered geometry.

2.2. ***Molecular Dynamics configurations***

The dependence of δ on the particle size is here investigated for two classes of nanoscale geometries, namely carbon nanotubes and biomolecules. The variety of the considered sample allows to explore hydrophobic and hydrophilic surfaces, inorganic molecules and biomolecules as well as biomolecules with different biological functions, for a broader generalization of results.

In particular, CNTs with (10,10) chirality (i.e. 1.36 nm diameter) and length spanning from 1 to 200 carbon rings (i.e. from $\approx$0.25 to $\approx$49 nm) are simulated, with geometries generated by VMD software [39]. On the other hand, 5 different proteins, 1 polipeptide, 13 amino acids and arrays of amino acids are investigated, to provide biomolecules with different size, aspect ratio and surface chemistry. Specifically, the proteins taken into account are: B1 Immunoglobulin binding-domain, 1PGB; Ubiquitin, 1UBQ; Green Fluorescence protein, 1QXT; Lysozime, 1AKI; Leptine, 1AX8. Instead, the 13 amino acids

considered are: Arginine (ARG), Aspartic Acid (ASP), Glutamic Acid (GLU) and Lysine (LYS) among charged amino acids; Asparagine (ASN), Glutamine (GLN), Serine (SER), Threonine (THR) and Tyrosine (TYR) within the polar group and Valine (VAL), Isoleucine (ISO), Leucine (LEU) and Glycine (GLY) for the neutral family. Furthermore, a folded chain of ten amino acids (UAO polipeptide [40]) has been also simulated, as it represents a link between simple amino acid molecules and complex proteins. The geometries of biomolecules have been taken from the RCSB Protein Data Bank [41], and further details can be found elsewhere [37].

Both bonded (bond stretching, angle and dihedral potentials) and nonbonded (Lennard-Jones and Coulomb potentials) interactions are considered for the MD configurations. Carbon-carbon interactions in the CNT structure are mimicked by two harmonic terms, whereas nonbonded interactions between water molecules and CNTs are modeled by 12-6 Lennard-Jones potential [42, 43, 44, 45]. Bonded and nonbonded interactions of biomolecules are modeled by CHARMM27 force field [46, 47].

Knowing the particle geometry and the solid-water nonbonded interactions, δ can be simply computed by the protocol provided in Reference [1], once the Connolly surface [38] of solid molecules is calculated from MD trajectories. To this end, the solid particles are first fully solvated in a dodecahedral box, where the solvent molecules are described by SPC/E model [48]. Note that the neutrality of the systems is achieved by adding Cl^- or Na^+ ions, when needed. After the energy minimization of the structure, two equilibration steps of 100 ps each are then performed: the former is carried out in a canonical ensemble (NVT, 300 K) by coupling a velocity rescaling thermostat to the system [49]; the latter is performed in a isothermal-isobaric ensemble (NPT, 300 K and 1 bar) by means of Parrinello-Rahman barostat [50, 51]. Finally, a 1 ns simulation is performed on the equilibrated system, in order to measure the solvent accessible surface of the structure at steady state conditions. MD simulations and post-processing are performed by GROMACS software [52]. Further details of the simulation procedure can be found elsewhere [1, 37].

3. Results

First, CNTs with fixed diameter ($\phi = 1.36$ nm) but different length (L from 0.25 to 49 nm) are considered (Figure 1a). As expected, SAS linearly increases with CNT length, namely from 9.24 ($L = 0.25$ nm) to 405.18 ($L = 49$ nm) nm^2. On the other hand, the characteristic length of the water nanolayer shows lower values with short CNTs (e.g. $\delta = 0.21$ nm for $SAS = 9.23$ nm^2), whereas it tends to exponentially converge to $\delta = 0.37$ nm with longer CNTs (Figure 1b). MD results shown in Figure 1b can be then accurately fitted ($R^2 = 0.99$) by a semi-empirical law:

$$\delta = \delta_0 \exp\left(-\frac{a}{SAS^b}\right), \tag{6}$$

where $a = 9.13$ and $b = 1.27$ are fitting parameters (SAS is expressed in nm^2), while $\delta_0 = 0.37$ nm is the asymptotic value of δ with infinitely long CNTs. Error bars in Figure 1b are derived from the standard deviations of local SAS with time, and the maximum relative error is 5%. Therefore, results show a clear size dependence of δ on the CNT length, at least for CNTs with SAS approximately smaller than 100 nm^2.

Second, the hydration layer thickness around the simulated 5 proteins and 13 amino acids have been already tabulated in Reference [37]; here, the analysis is further extended to ordered arrays of amino acids and a polipeptide. This allows to systematically detect how the hydration layer thickness changes by gradually increasing the size of biomolecules. Three array configurations are analyzed: 4 ARG molecules arranged in a 2x2 matrix (Figure 2a), 9 ARG in a 3x3 array (Figure 2c) and 16 ARG in a 4x4 matrix. The distance between the center of mass of adjacent Arginines is fixed to 0.3 nm, such that water molecules cannot penetrate within the interspaces between contiguous ARG. Hence, each array configuration actually mimics a compact biomolecule. Figure 2d shows that the resulting solvent accessible surface of the array (black squares) increases with the amount of amino acids (#ARG), even though a progressive SAS overlap can be also observed. In fact, the blue dotted line in Figure 2d represents SAS = #ARG $\times$ SAS$_{\mathrm{ARG}}$, where SAS$_{\mathrm{ARG}}$ is the solvent accessible surface of a single,

isolated ARG. Figure 2b, instead, confirms that the water confining capability of ARG arrays increases with their size (i.e. #ARG thus overall SAS), and it eventually tends to 0.30 nm, namely the average value found for proteins [37] (green dot-dashed line). A maximum value of 0.29 nm is obtained for the 16 ARG array. This trend is further supported by the water confining potential measured for the UAO polipeptide (1UAO [40]): UAO shows SAS = 10.15 nm^2 and $\delta = 0.25$ nm.

The δ and SAS collected for proteins, amino acids, ARG arrays and the UAO polipeptide are then grouped in Figure 3, where the characteristic length of water nanolayer is plotted as a function of the corresponding solvent accessible surface. Results show that, as previously demonstrated in the CNT case, also biomolecules exhibit a size dependence for δ, particularly evident for SAS < 20 nm^2. The trend in Figure 3 is obtained by fitting results with the semi-empirical model shown in Equation 6 ($R^2 = 0.98$). In the case of biomolecules, the fitting parameters are $a = 1.13$ and $b = 0.72$, while $\delta_0 = 0.32$ nm is the asymptotic value of δ in case of large proteins. Error bars in Figure 3 are derived from the standard deviations of local SAS with time, and they are always lower than $1.5 \cdot 10^{-2}$ nm.

Therefore, the hydration layer at solid-liquid interface is related to the molecule size below a characteristic geometric dimension (e.g. $SAS \approx 100$ nm^2 for CNTs; SAS ≈ 20 nm^2 for biomolecules), at which δ starts decreasing with the molecule size. Above this limit, instead, the depth of hydration layer only depends on the physical-chemical characteristics of the solid surface [1, 37], being size independent.

As an example, the hydrophilic behavior of charged and polar amino acids is stronger than that of neutral ones. The different water affinity is due to the amount of hydrogen bonds (#HB) between water molecules and amino acids. Figure 4 demonstrates that charged (Arginine) and polar (Asparagine) amino acids are more prone to form hydrogen bonds with water molecules (≈ 11 and ≈ 9 #HB, respectively) than neutral amino acids (Isoleucine, ≈ 7 #HB). This behavior clearly affects also the thickness of the hydration layer. In fact, charged

or polar residues imply a deeper potential well (U_{eff}) and thus a stronger water confinement at the solid-liquid interfaces. As confirmed by the values of δ reported in [37], amino acids with similar SAS but different water affinity show significantly different δ: for example, ASP (charged) and VAL (neutral) have $\delta = 0.18$ nm and 0.15 nm respectively, that is 20% difference.

4. Discussion

Both CNTs and biomolecules have shown a clear dependence of water nanolayer on particle size. This result can be explained by recalling that δ is computed from the local solid-liquid effective potential. To this purpose, five CNTs with different length are considered, namely $L = 0.5$, 2, 3.7, 24.6 and 49 nm. For each case, U_{eff} is calculated along the direction $\mathbf{n}$ normal to one of the carbon atoms located at $\frac{L}{2}$ (see Figure 5a). Figure 5b shows that the water confining potential exerted by the considered atom tends to be progressively stronger as the CNT length increases, eventually reaching a plateau value for long CNTs. This confirms the trend of hydration layer thickness in Figure 1: below a characteristic size, the thickness of hydration layer, i.e. the attractive potential felt by water molecules at the solid-liquid interface, depends on the dimension of nanoconstructs.

In our previous work [37], we suggested that the size dependence of δ stems from the superposition of nonbonded interactions. There, δ was investigated for a couple of Arginine molecules at decreasing distance. By reducing the distance between contiguous ARG molecules, more atoms were considered within the cut-off radius and the superposition of nonbonded interactions progressively became more intense thus causing an enhanced attraction of the surrounding water molecules. Consequently, the depth of hydration layer was larger than in case of a single, isolated ARG molecule. This simple demonstration allows to understand why extremely small molecules are characterized by a weaker water absorption effect. Similarly, the superposition of solid-liquid interaction potentials is the mechanism underlying the size dependence of δ also in CNTs,

as evident in Figures 1 and 5.

The reported results demonstrate that the size dependence of δ is a consequence of the limited amount of solid atoms participating to the interaction potentials with surrounding water molecules, and such dependence eventually plateaus above a characteristic molecule size. Hence, despite the nanolayer thickness δ only depends on the surface properties of the confining surface, size effects must be also taken into account in case of small nanostructures.

5. Conclusions

The study of water dynamics at solid-liquid interfaces has strong implications in several research fields. The peculiar behavior of water molecules in the proximity of solid nanostructures influences both the overall properties of liquid and the dynamics of solid particles. In this work, molecular dynamics simulations and theoretical considerations have been carried out to evaluate the characteristic length of water nanolayer δ. Such quantity can be considered as the distance normal to the solid surface below which solid-liquid nonbonded interactions prevail on the kinetic energy of the fluid, thus causing the characteristic reduced fluid mobility in the nanolayer.

Here, the dependence of δ with the solid molecules size has been investigated. Two nanoscale geometries have been taken into account, namely carbon nanotubes with different lengths and biomolecules (i.e. proteins, polipeptides and amino acids) with varied dimensions. Results demonstrate a general size dependence of the confined water thickness: δ decreases by reducing the solid particle dimension, i.e. either CNT length or solvent accessible surface of biomolecules. However, there exists a characteristic size threshold above which the hydration layer depth is only dependent on the physical-chemical surface properties of the solid molecules. The origin of this size effect is found in the superposition principle for the solid-liquid nonbonded potentials. In fact, in case of small solid particles (i.e. CNTs shorter than 10 nm; biomolecules with SAS < 20 nm^2), the limited amount of atoms participating to nonbonded interactions with water

molecules causes a weak overall attractive potential at the solid-liquid interface, thus a reduced hydration layer is formed.

In conclusion, the thickness of nanoconfined water at the solvent-particle interface is generally affected by physical-chemical properties of the solid surface; however, it is also strongly dependent on the particle dimension, at least below a certain size threshold. The behavior of interfacial water depth as function of biomolecule size could predict some self-assembly and structural phenomena occurring in the biomedical field. For example, the dynamics of water in the first hydration shell plays an important role in the structural stability of amyloid-$\beta(1-40)$ peptide, whose agglomeration is thought to be the main responsible of the Alzheimer disease [53]. Hence, the evaluation of δ values during the agglomeration phenomena may predict (and prevent) the formation and growth of bigger amyloidal plaques. Moreover, the structural changes of dioleoylphosphatidylcholine (DOPC) bilayer and the solubilization of cholesterol crystallites promoted by their progressive hydration may be explained by recalling the sensitivity of the hydration layer depth on the particle dimension [32, 54]. The particle size dependence of δ could also have interesting implications in the engineering sector. Several studies already highlight that the clustering and aggregation dynamics of suspended nanoparticles are influenced by the hydration layer depth at the interface [35, 36]. Hence, a precise and quantitative analysis of the thickness of nanolayer in relation to the solid particle dimension may guide a more rational design of nanoparticle suspensions avoiding clustering phenomena, which are the real bottleneck to a more widespread industrial application of engineered nanosuspensions.

Acknowledgments

Authors would like to acknowledge the NANO-BRIDGE – Heat and mass transport in NANO-structures by molecular dynamics, systematic model reduction, and non-equilibrium thermodynamics (PRIN 2012, grant number 2012LHPSJC) and the NANOSTEP – NANOfluid-based direct Solar absorption for

Thermal Energy and water Purification (Fondazione CRT, Torino) projects. Authors thank CINECA (Iscra C project COGRAINS) and the computational resources provided by HPC@POLITO (`http://www.hpc.polito.it`).

References

[1] E. Chiavazzo, M. Fasano, P. Asinari, P. Decuzzi, Scaling behaviour for the water transport in nanoconfined geometries, Nature communications 5 (2014) 4495.

[2] B. Bagchi, Water dynamics in the hydration layer around proteins and micelles, Chemical Reviews 105 (9) (2005) 3197–3219.

[3] P. Gallo, M. Rovere, E. Spohr, Supercooled confined water and the mode coupling crossover temperature, Physical review letters 85 (20) (2000) 4317.

[4] G. Ruppeiner, P. Mausbach, H.-O. May, Thermodynamic r-diagrams reveal solid-like fluid states, Physics Letters A 379 (7) (2015) 646–649.

[5] S. H. Khan, G. Matei, S. Patil, P. M. Hoffmann, Dynamic solidification in nanoconfined water films, Physical review letters 105 (10) (2010) 106101.

[6] M. P. Goertz, J. Houston, X.-Y. Zhu, Hydrophilicity and the viscosity of interfacial water, Langmuir 23 (10) (2007) 5491–5497.

[7] P.-A. Mante, C.-C. Chen, Y.-C. Wen, H.-Y. Chen, S.-C. Yang, Y.-R. Huang, I.-J. Chen, Y.-W. Chen, V. Gusev, M.-J. Chen, et al., Probing hydrophilic interface of solid/liquid-water by nanoultrasonics, Scientific reports 4 (2014) 6249.

[8] U. Raviv, J. Klein, Fluidity of bound hydration layers, Science 297 (5586) (2002) 1540–1543.

[9] D. Ortiz-Young, H.-C. Chiu, S. Kim, K. Voïtchovsky, E. Riedo, The interplay between apparent viscosity and wettability in nanoconfined water, Nature communications 4 (2013) 2482.

[10] B. Kim, S. Kwon, H. Mun, S. An, W. Jhe, Energy dissipation of nanoconfined hydration layer: Long-range hydration on the hydrophilic solid surface, Scientific reports 4 (2014) 6499.

[11] M. Fasano, D. Borri, E. Chiavazzo, P. Asinari, Protocols for atomistic modeling of water uptake into zeolite crystals for thermal storage and other applications, Applied Thermal Engineering.

[12] G. Hummer, J. C. Rasaiah, J. P. Noworyta, Water conduction through the hydrophobic channel of a carbon nanotube, Nature 414 (6860) (2001) 188–190.

[13] S. O. Diallo, Pore-size dependence and characteristics of water diffusion in slitlike micropores, Phys. Rev. E 92 (2015) 012312.

[14] N. Osti, A. Coté, E. Mamontov, A. Ramirez-Cuesta, D. Wesolowski, S. Diallo, Characteristic features of water dynamics in restricted geometries investigated with quasi-elastic neutron scattering, Chemical Physics 465 (2016) 1–8.

[15] M. Fasano, E. Chiavazzo, P. Asinari, Water transport control in carbon nanotube arrays, Nanoscale research letters 9 (1) (2014) 1–8.

[16] T. Humplik, R. Raj, S. Maroo, T. Laoui, E. N. Wang, Effect of hydrophilic defects on water transport in MFI zeolites, Langmuir 30 (22) (2014) 6446–6453.

[17] A. Gizzatov, J. Key, S. Aryal, J. Ananta, A. Cervadoro, A. L. Palange, M. Fasano, C. Stigliano, M. Zhong, D. Di Mascolo, A. Guven, E. Chiavazzo, P. Asinari, X. Liu, M. Ferrari, L. J. Wilson, P. Decuzzi, Hierarchically structured magnetic nanoconstructs with enhanced relaxivity and cooperative tumor accumulation, Advanced Functional Materials 24 (29) (2014) 4584–4594.

[18] A. Mukherjee, R. Lavery, B. Bagchi, J. T. Hynes, On the molecular mechanism of drug intercalation into dna: a simulation study of the intercalation

pathway, free energy, and dna structural changes, Journal of the American Chemical Society 130 (30) (2008) 9747–9755.

[19] B. Nguyen, S. Neidle, W. D. Wilson, A role for water molecules in dna- ligand minor groove recognition, Accounts of chemical research 42 (1) (2008) 11–21.

[20] L. Xue, P. Keblinski, S. Phillpot, S.-S. Choi, J. Eastman, Effect of liquid layering at the liquid–solid interface on thermal transport, International Journal of Heat and Mass Transfer 47 (19) (2004) 4277–4284.

[21] G. Balasubramanian, S. Sen, I. K. Puri, Shear viscosity enhancement in water–nanoparticle suspensions, Physics Letters A 376 (6) (2012) 860–863.

[22] S. Murshed, K. Leong, C. Yang, Thermophysical and electrokinetic properties of nanofluids, a critical review, Applied Thermal Engineering 28 (17) (2008) 2109–2125.

[23] A. Cervadoro, M. Cho, J. Key, C. Cooper, C. Stigliano, S. Aryal, A. Brazdeikis, J. F. Leary, P. Decuzzi, Synthesis of multifunctional magnetic nanoflakes for magnetic resonance imaging, hyperthermia, and targeting., ACS applied materials & interfaces 6 (15) (2014) 12939–12946.

[24] H.-X. Zhou, G. Rivas, A. P. Minton, Macromolecular crowding and confinement: biochemical, biophysical, and potential physiological consequences, Annual review of biophysics 37 (2008) 375.

[25] R. J. Ellis, A. P. Minton, Cell biology: join the crowd, Nature 425 (6953) (2003) 27–28.

[26] A. R. Bizzarri, S. Cannistraro, Flickering noise in the potential energy fluctuations of proteins as investigated by md simulation, Physics Letters A 236 (5) (1997) 596–601.

[27] C. Manetti, A. Giuliani, M.-A. Ceruso, C. L. Webber, J. P. Zbilut, Recurrence analysis of hydration effects on nonlinear protein dynamics: multi-

plicative scaling and additive processes, Physics Letters A 281 (5) (2001) 317–323.

[28] R. B. Best, G. Hummer, Diffusive model of protein folding dynamics with kramers turnover in rate, Physical review letters 96 (22) (2006) 228104.

[29] A. Fernández, H. A. Scheraga, Insufficiently dehydrated hydrogen bonds as determinants of protein interactions, Proceedings of the National Academy of Sciences 100 (1) (2003) 113–118.

[30] N.-V. Buchete, G. Hummer, Structure and dynamics of parallel β-sheets, hydrophobic core, and loops in alzheimers aβ fibrils, Biophysical journal 92 (9) (2007) 3032–3039.

[31] A. De Simone, G. G. Dodson, C. S. Verma, A. Zagari, F. Fraternali, Prion and water: tight and dynamical hydration sites have a key role in structural stability, Proceedings of the National Academy of Sciences of the United States of America 102 (21) (2005) 7535–7540.

[32] G. Caracciolo, D. Pozzi, R. Caminiti, Hydration effect on the structure of dioleoylphosphatidylcholine bilayers, Applied physics letters 90 (18) (2007) 183901.

[33] M. Ahmad, W. Gu, T. Geyer, V. Helms, Adhesive water networks facilitate binding of protein interfaces, Nature communications 2 (2011) 261.

[34] I. Son, Y. L. Shek, D. N. Dubins, T. V. Chalikian, Hydration changes accompanying helix-to-coil dna transitions, Journal of the American Chemical Society 136 (10) (2014) 4040–4047.

[35] J. Israelachvili, H. Wennerström, Role of hydration and water structure in biological and colloidal interactions, Nature 379 (1996) 219.

[36] W. Lv, R. Wu, The interfacial-organized monolayer water film (mwf) induced two-step aggregation of nanographene: both in stacking and sliding assembly pathways, Nanoscale 5 (7) (2013) 2765–2775.

[37] A. Cardellini, M. Fasano, E. Chiavazzo, P. Asinari, Mass transport phenomena at the solid-liquid nanoscale interface in biomedical application, in: VI International Conference on Computational Methods for Coupled Problems in Science and Engineering COUPLED PROBLEMS 2015, 2015, pp. 593–604.

[38] F. Eisenhaber, P. Lijnzaad, P. Argos, C. Sander, M. Scharf, The double cubic lattice method: efficient approaches to numerical integration of surface area and volume and to dot surface contouring of molecular assemblies, Journal of Computational Chemistry 16 (3) (1995) 273–284.

[39] W. Humphrey, A. Dalke, K. Schulten, Vmd: visual molecular dynamics, Journal of molecular graphics 14 (1) (1996) 33–38.

[40] S. Honda, K. Yamasaki, Y. Sawada, H. Morii, 10 residue folded peptide designed by segment statistics, Structure 12 (8) (2004) 1507–1518.

[41] H. M. Berman, J. Westbrook, Z. Feng, G. Gilliland, T. Bhat, H. Weissig, I. N. Shindyalov, P. E. Bourne, The protein data bank, Nucleic acids research 28 (1) (2000) 235–242.

[42] Y. Quo, N. Karasawa, W. A. Goddard, Prediction of fullerene packing in C60 and C70 crystals, Nature 351 (1991) 464–467.

[43] J. H. Walther, R. Jaffe, T. Halicioglu, P. Koumoutsakos, Carbon nanotubes in water: structural characteristics and energetics, The Journal of Physical Chemistry B 105 (41) (2001) 9980–9987.

[44] E. Chiavazzo, P. Asinari, Enhancing surface heat transfer by carbon nanofins: towards an alternative to nanofluids?, Nanoscale research letters 6 (1) (2011) 1–13.

[45] M. Fasano, M. B. Bigdeli, M. R. Sereshk Vaziri, E. Chiavazzo, P. Asinari, Thermal transmittance of carbon nanotube networks: Guidelines for novel thermal storage systems and polymeric material of thermal interest, Renewable & Sustainable Energy Reviews 41 (2015) 1028–1036.

[46] A. D. MacKerell, D. Bashford, M. Bellott, R. Dunbrack, J. D. Evanseck, M. J. Field, S. Fischer, J. Gao, H. Guo, S. Ha, et al., All-atom empirical potential for molecular modeling and dynamics studies of proteins, The Journal of Physical Chemistry B 102 (18) (1998) 3586–3616.

[47] A. D. MacKerell, M. Feig, C. L. Brooks, Extending the treatment of backbone energetics in protein force fields: Limitations of gas-phase quantum mechanics in reproducing protein conformational distributions in molecular dynamics simulations, Journal of computational chemistry 25 (11) (2004) 1400–1415.

[48] H. Berendsen, J. Grigera, T. Straatsma, The missing term in effective pair potentials, Journal of Physical Chemistry 91 (24) (1987) 6269–6271.

[49] G. Bussi, D. Donadio, M. Parrinello, Canonical sampling through velocity rescaling, The Journal of chemical physics 126 (1) (2007) 014101.

[50] M. Parrinello, A. Rahman, Polymorphic transitions in single crystals: A new molecular dynamics method, Journal of Applied physics 52 (12) (1981) 7182–7190.

[51] S. Nosé, M. Klein, Constant pressure molecular dynamics for molecular systems, Molecular Physics 50 (5) (1983) 1055–1076.

[52] B. Hess, C. Kutzner, D. Van Der Spoel, E. Lindahl, Gromacs 4: algorithms for highly efficient, load-balanced, and scalable molecular simulation, Journal of chemical theory and computation 4 (3) (2008) 435–447.

[53] F. Massi, J. E. Straub, Structural and dynamical analysis of the hydration of the alzheimer's β-amyloid peptide, Journal of computational chemistry 24 (2) (2003) 143–153.

[54] D. Pozzi, R. Caminiti, C. Marianecci, M. Carafa, E. Santucci, S. C. De Sanctis, G. Caracciolo, Effect of cholesterol on the formation and hydration behavior of solid-supported niosomal membranes, Langmuir 26 (4) (2009) 2268–2273.

Figures

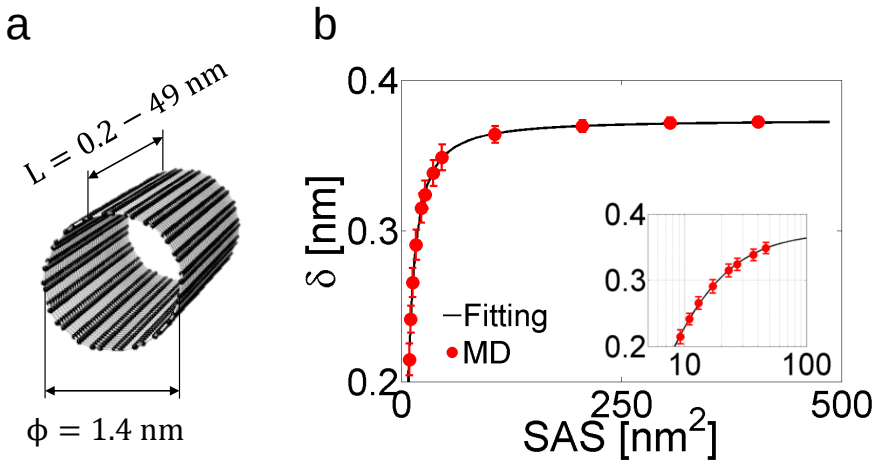

Figure 1: Size dependence of δ for CNTs. **(a)** Geometrical parameters of the simulated CNTs. Note that water molecules wet both inner and outer surface of the simulated CNTs. **(b)** Characteristic length of nanolayer (δ) for CNTs with different Solvent Accessible Surface (SAS). The inset highlights (logarithmic x axis) the trend of δ with $SAS < 100$ nm^2. MD results (dots) are fitted by the semi-empirical model shown in Equation 6.

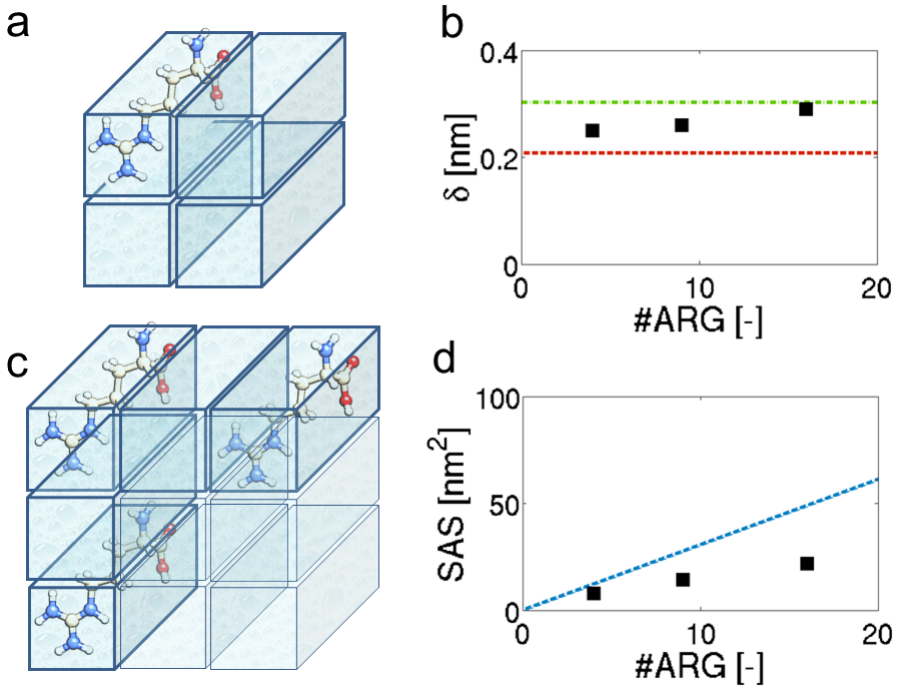

Figure 2: δ and SAS for Arginine arrays. **(a)** Arrays of 4 and **(c)** 9 ARG, where each blue parallelepiped represents an Arginine molecule. Note that some ARG are not visualized for better clarity. **(b)** δ in case of 4, 9 and 16 ARG arrays (black squares). The green dot-dashed line depicts the average δ for the simulated proteins; whereas the red dashed line the average δ for the considered amino acids. **(d)** SAS in case of the ARG arrays (black squares). Note that the blue dotted line is obtained as SAS = #ARG $\times$ SAS$_{\mathrm{ARG}}$, where SAS $_{\mathrm{ARG}}$ is the solvent accessible surface of a single, isolated ARG.

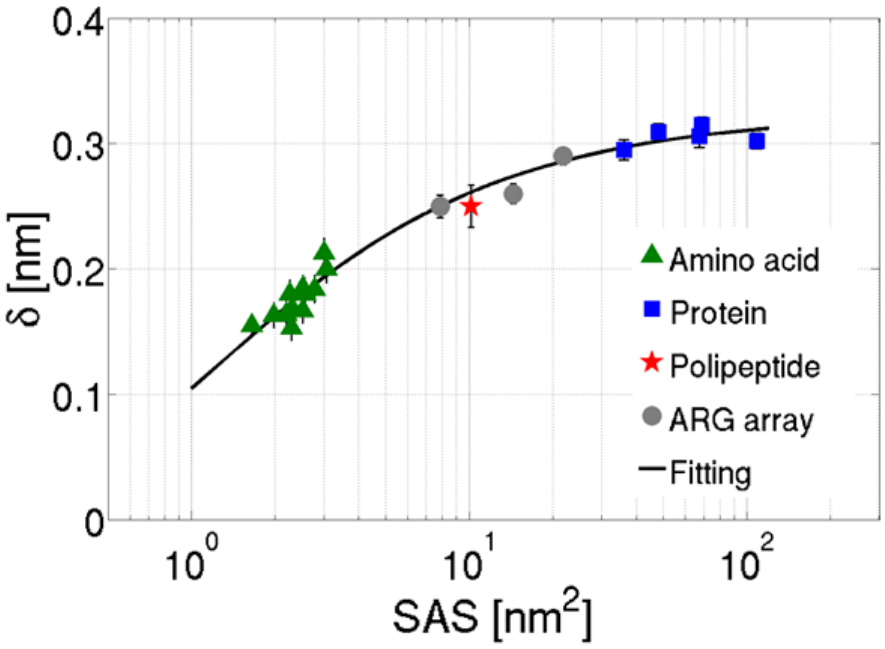

Figure 3: δ-SAS relation for the considered biomolecules. The simulated proteins (blue squares [37]), Arginine arrays (gray dots, see Figure 2), polipeptide (red star, as from Reference [40]) and amino acids (green triangles, [37]) are depicted. MD results (dots) are fitted by the semi-empirical model shown in Equation 6

.

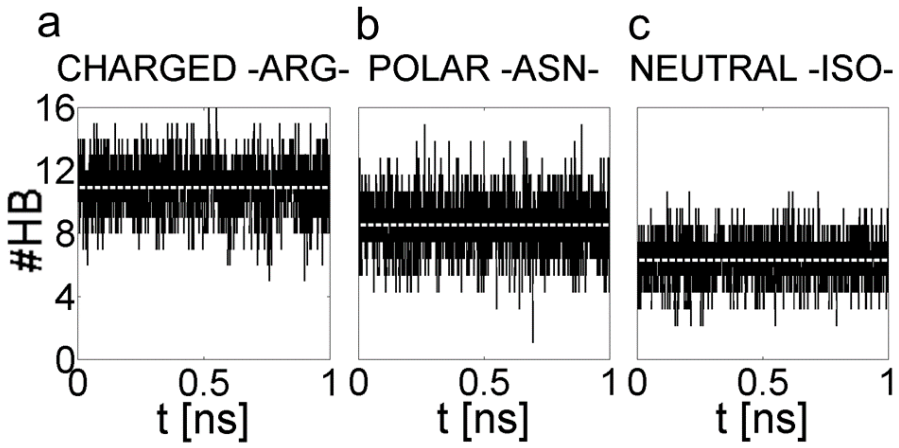

Figure 4: Average number of hydrogen bonds (#HB) during MD simulations. **(a)** Arginine (charged group). **(b)** Asparagine (polar group). **(c)** Isoleucine (neutral group). The white dashed lines indicate the mean #HB value.

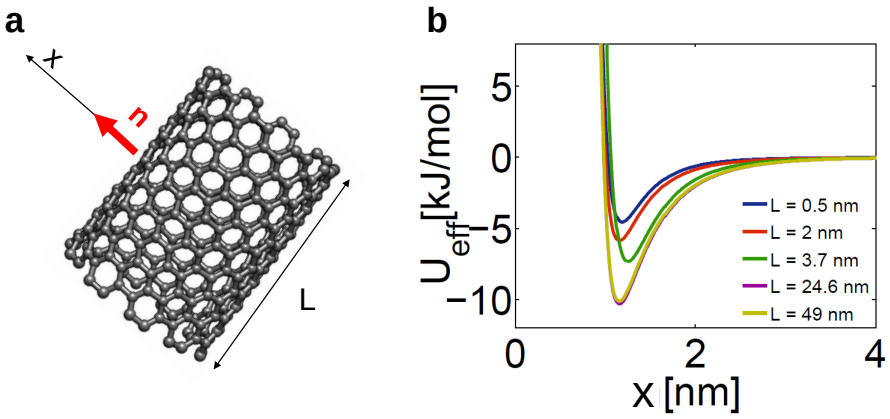

Figure 5: Local effective potential for CNTs. **(a)** The normal direction, **n**, on the solvent accessible surface of a CNT is represented. **(b)** For each CNT length (L), a carbon atom located at $\frac{L}{2}$ is considered, and the effective potential U_{eff} is calculated along the direction x, which is normal to the local SAS.